Int J Adv Manuf Technol (2017) 89:735–742
DOI 10.1007/s00170-016-9102-6

CrossMark

ORIGINAL ARTICLE

Phase and stress evolution of Si swarf in the diamond-coated wire sawing of Si ingots

Sriya Banerjee[1] · Junting Yang[1] · Junnan Wu[1,4] · Michelle Heredia[3] · Zhengning Gao[2] · Yoon Myung[1] · Omid Rezvanian[4] · Parag Banerjee[1,2]

Received: 23 March 2016 / Accepted: 26 June 2016 / Published online: 9 July 2016
© Springer-Verlag London 2016

Abstract
Diamond-coated wire (DCW) sawing of Si solar ingots generates swarf which is analyzed using micro-Raman spectroscopy. Two types of Si swarf are found. Particulate swarf is crystalline and shows residual compressive stress. Fibrillar swarf is amorphous and shows residual tensile stress. The origin of particulate, crystalline swarf is attributed to brittle machining, while the origin of fibrillar, amorphous swarf is attributed to ductile machining. Finite element modeling suggests that brittle machining resulting in particulate, crystalline swarf generation is initiated by sharp diamond microparticles. On the other hand, ductile machining resulting in fibrillar, amorphous swarf generation is caused by blunt diamond microparticles. Over the course of sawing, the ratio of crystalline/amorphous phase in swarf decreases, quantifying the average loss in sharpness of diamond microparticles. Thus, micro-Raman spectroscopy can be an effective analytical tool for quantifying and monitoring DCW sawing processes for Si solar ingots.

✉ Parag Banerjee
parag.banerjee@wustl.edu

[1] Department of Mechanical Engineering and Materials Science, Washington University in St. Louis, One Brookings Drive, St. Louis, MO 63130, USA

[2] Institute of Materials Science and Engineering, Washington University in St. Louis, One Brookings Drive, St. Louis, MO 63130, USA

[3] Energy, Environmental and Chemical Engineering, Washington University in St. Louis, One Brookings Drive, St. Louis, MO 63130, USA

[4] SunEdison, 501 Pearl Drive, St. Peters, MO 63376, USA

Keywords Swarf · Diamond-coated wire sawing · Si ingots

1 Introduction

Si wafering in photovoltaic (PV) manufacturing accounts for 11 % of final module cost [1]. Therefore, cost savings realized at this process step significantly impacts the $/Watt of PV modules. Diamond-coated wire (DCW) sawing [2] of Si ingots aims to minimize wafering costs with concurrent advantages of higher cutting rates and significantly less environmental impact through minimal use of cutting fluid [3,4].

The process of DCW sawing is highly complex and is depicted in Fig. 1a. Diamond microparticles are attached to a steel wire, i.e., core, 100 μm in diameter (Fig. 1a, inset). The wire is weaved around a series of wire guide rollers forming a webbed frame. The entire wire is wound on two spools ("feed" and "draw"). The wire can travel at speeds of up to 25 m/s, cutting grooves leading to slicing of Si ingot into wafers.

As shown in Fig. 1b, diamond microparticles at any given time are either in contact with regions "A" and "B" or face the groove created by the cut or "kerf." Brittle fractures are preferable for faster cutting in A. This generates the first source of Si waste, or "swarf." Ductile cutting is preferable for smoother wafer surfaces (and lower depth of damage on the wafer) in B. This generates a second source of swarf. These opposing requirements of brittle and ductile machining during DCW sawing make the process challenging to understand, control, and model.

While diamond machining of Si under brittle and ductile modes has been studied [5–11], these pertain to single diamond cutting tools on standard machining platforms such as lathes where the tool tip geometries are predefined and precisely controlled. Brittle and ductile modes of Si removal on a

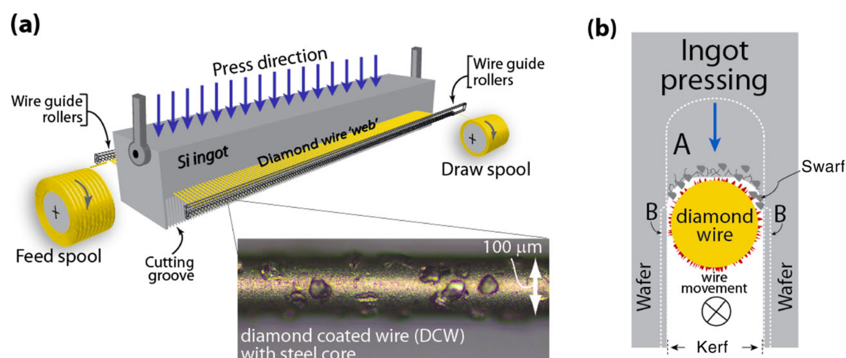

Fig. 1 **a** Schematic of the DCW sawing process with inset showing the DCW with embedded diamonds on a steel wire core 100 μm in diameter. **b** Cross section of a Si kerf showing regions *A* and *B* from where Si swarf production originates. The diamond wire is moving into the plane of the paper

wafer have been elucidated as well [12,13]. When the undeformed chip thickness from Si is less than the diamond microparticle tip radius, ductile chip formation occurs [14]. When a tool tip either (1) roughens with asperities on its surface or (2) the depth of cut is increased, brittle modes become dominant [8, 15]. These investigations, though critical to understanding ductile Si machining, are not representative of cutting in a DCW environment where a multitude of diamonds performs the cut and hence necessitates the need for studying the ensemble behavior of many diamonds.

There are relatively few papers in literature on DCW sawing of Si wafers [2,3,16–20]. Here, most of the studies are focused on the Si wafers produced and none of them pertain to the study of Si swarf. Our group has shown previously that the individual diamond microparticles attached to the cutting wire undergo stress and phase transformation during DCW sawing [20]. However, Si swarf has not been studied yet. Such studies can lead to better understanding of the DCW sawing process, minimal swarf production, and hence, reduced operating costs.

Therefore, in this paper, we study the Si swarf and track its fundamental material property—crystallinity—that evolves over the entire period of cutting. In order to ascertain the Si swarf crystallinity, we use an analytical technique called micro-Raman spectroscopy. Micro-Raman spectroscopy serves as a sensitive tool for detecting built-in stresses and changes to structure in Si [21]. This is because Si has a strong Raman peak at 520 cm^{-1} corresponding to the first-order optical phonon modes of a Si-Si bond. When stressed, this peak shifts by a few wavenumbers and/or develops other peaks such as those of metallic, metastable, and/or amorphous Si phases [22].

In this study, we find the presence of both particulate and fibrillar Si particles in the swarf. The crystallinity and local stress signatures of individual particles are characterized. The Raman signatures of the collective swarf powder are studied, and volume fraction of particulate/fibrillar particles in the swarf is parameterized. The evolution of Raman characteristics of the swarf allows us to understand the interaction of a multitude of diamond microparticles with the Si ingot, as wafering proceeds from beginning until the end.

2 Experimental

Si swarf was obtained from SunEdison® Inc. A Meyer Burger DS-271 DCW industrial sawing machine was used to cut monocrystalline Si ingot with a cross section of 15 cm × 15 cm. The Si swarf was collected at the beginning and end of the sawing process which was 8 h long. The cutting was done at a constant feed rate of 5 μm/s. The average wire velocity is maintained at 15 m/s. The diamond particles embedded on the DCW had a nominal diameter of 12 μm with a 1 standard deviation spread in size of ±6 μm.

The as-received Si swarf was in a mixture of cooling liquid, which contained water and a proprietary surfactant. To separate Si swarf from the cooling liquid, the mixed solution was centrifuged at 8000 rpm for 10 min. In order to obtain individual Si particles, 0.0010 g Si swarf was dispersed into 10-mL ethanol. After sonicating for 5 min, 10 μL of this diluted solution was drop-casted on an Al foil. This sample was used for making Raman measurements ensuring the only Si signal came from the individual swarf particles. A JEOL 7100FLV Field Emission scanning electron microscope (SEM) was used to study the morphology of individual Si particles.

A Renishaw® InVia micro-Raman confocal spectrometer was used for making all Raman measurements on the Si swarf. Laser excitation at 785 nm (power = 2.467 mW/cm^2) was applied, with laser spot size of 0.83 and 1.3 μm in diameter, respectively. Unless otherwise noted, an objective of 50× was used to collect data resulting in a numerical aperture (NA) of 0.75. Scans were conducted from 100 to 3200 cm^{-1}. The exposure time for every scan was 10 s. Every scan was integrated once. The grating used was 1200 lines/mm for a 785-nm laser source. All measurements were calibrated first using the Si I diamond cubic, TO phonon peak

at 520 cm^{-1} originating from a Si prime, single side polished, wafer surface.

3 Finite element modeling

A 2D plain strain, finite element model of a rigid sharp indenter on a flat surface representing diamond grit on a monocrystalline Si workpiece was used to illustrate the relationship between sharpness of the indenter and stress fields developed around the indenter in Si. The radius of the indenter tip, c, is taken as a measure for sharpness of the indenter and is varied from 0.1 to 0.8 μm. Indenter's height, h, is assumed to be 3 μm. In order to exclude the effect of indenter tip angle, α, it is assumed to be constant in all cases and equal to 26.57°. This angle is within the range of diamond microparticles encountered on a DCW. The Si workpiece is represented by a 8 μm × 3 μm rectangle. Based on a convergence analysis, an element size of 0.02 μm is chosen. Also, due to symmetry around the y-axis, only half of the geometry is modeled. The indenter is moved down by 0.01 μm as a rigid body, while nodal displacements at the bottom of the Si piece are constrained in y direction. Simulations are performed in ANSYS 15®. The contact stiffness is chosen such that maximum contact penetration remains less than 2.5 % of element size. Elastic modulus and Poisson's ratio for Si are assumed to be 130 GPa and 0.28, respectively [23].

4 Results and discussion

4.1 SEM of individual Si swarf particles

Two types of particles were found in the Si swarf. A representative image is shown in the SEM in Fig. 2a where both "particulate" Si and "fibrillar" Si are observed. The particulate Si is ~100 nm in diameter. Alternately, fibrillar Si 200–300 nm wide and 3–5 μm long is observed as well. The criteria for ductile cutting is given as the undeformed chip thickness < diamond microparticle tip radius [14]. Thus, when the "depth of cut" is minimal, shear forces lead to cutting of Si. In this instance, diamond microparticle could be responsible for the fibrillar Si swarf as it "shaves off" material from the Si surface. Additionally, the hydrostatic pressure under the diamond tips has to be very high (10–13 GPa) such that metallic phase formation of Si is made possible [24]. In order to confirm this hypothesis, Raman spectra were obtained of the individual Si swarf particles.

4.2 Raman spectra of individual Si swarf particles

A representative spectrum of individual Si swarf particles is shown in Fig. 2b. The particulate Si (Fig. 2b, top) showed a sharp TO phonon peak corresponding to the diamond cubic structure of single crystalline Si [25]. However, its peak position at 522 cm^{-1} deviated from the unstressed Si peak which is reported to be 520 cm^{-1} [22,26]. The deviation, $\Delta\omega = 2\ cm^{-1}$ indicates compressive stresses in the particulate Si swarf [27]. While models are available linking Raman peak shifts to biaxial states of stress on a Si wafer [27,28], such assumptions cannot be made on Si swarf particles with irregular, 3D geometries. Hence, these results are interpreted qualitatively within the context of this paper.

The Raman spectra of the individual fibrillar Si swarf were very different. This is seen in Fig. 2b, bottom. Instead of a single peak, a series of peaks is observed. The spectra is deconvoluted into individual phases of Si namely, Si I diamond cubic (518 and 286 cm^{-1}), amorphous Si (480 cm^{-1}), and Si III and XII phases (351, 422, 435 cm^{-1}) [22]. These phases are related to the ductile machining mode of Si. It has

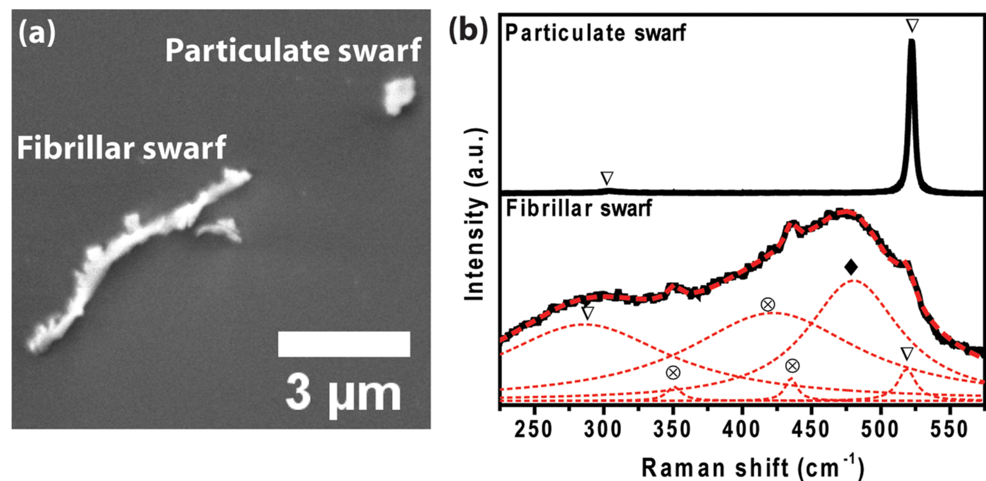

Fig. 2 **a** SEM of individual Si swarf particles showing particulate Si originating from a brittle cut, while fibrillar Si originating from a ductile cut. **b** Raman spectrum of particulate swarf (*top*) indicating crystalline, Si diamond cubic phase, and fibrillar swarf (*bottom*) showing three phases of Si: Si cubic (∇), amorphous Si (♦), and Si III/XII (⊗)

been reported [29] that under high pressures usually found under sharp diamond tips, the formation of a metallic Si phase (Si II) results in ductile machining. After cutting, high unloading rates cause the Si II to transform to Si III and Si XII. On the other hand, for low unloading rates, Si II transforms to amorphous Si [30]. Both amorphous Si, Si III, and Si XII indicate ductile machining of Si ingot, while the Si diamond cubic phase indicates that some crystallinity is still detected in the fibrillar swarf. Thus, a clear correlation between particle shape and its stress state and phase can be established with micro-Raman spectroscopy of the Si swarf.

4.3 Discerning trends in the Raman spectra of individual Si swarf particles

Nine Si individual particles with different morphologies were studied using Raman. Five of the nine Si particles were particulate-like, and four samples were fibrillar. The Raman spectrum of the individual particles is fitted with the Lorentzian fitting function. Two parameters of interest are extracted from these spectra. First, the peak position (Δω) of the Si TO phonon peak is noted. As indicated earlier, an upshift in this peak from 520 cm^{-1} indicates compressive stress in the particle, while a downshift indicates tensile stress. Second, the ratio of the intensity of the TO phonon peak to the intensity of the amorphous peak is extracted. This is given as $I_{cubic}/I_{amorphous}$. Thus, the higher this ratio, the higher is the crystalline component in the swarf particle and vice versa.

For the case where no cubic phase could be deconvoluted, $I_{cubic}/I_{amorphous}$ is taken to be 0.55, which is the ratio of intensity of the amorphous shoulder at 520 cm^{-1} (where the crystalline peak would have existed but could not be resolved) to the peak intensity of the amorphous peak at 480 cm^{-1}. Similarly, where only crystalline phase was observed, $I_{cubic}/I_{amorphous}$ is taken to be 180, the peak intensity of Si I, diamond cubic peak at 520 cm^{-1} (18,000 counts per second, cps) to background average signal (100 cps). We note that while these ratios may vary between systems and samples, the conclusions obtained are invariant to such changes.

The combined information from the two parameters, i.e., Δω vs. log ($I_{cubic}/I_{amorphous}$) is plotted in Fig. 3 as a "stress-phase" map. The horizontal dashed line at 520 cm^{-1} separates tensile from compressive stress. The vertical dashed line demarcates crystalline and amorphous regions where at this line, $I_{cubic} = I_{amorphous}$. Plotting the nine data points yields a trend, where only the first and third quadrants are populated. For particulate Si swarf which is crystalline, the residual stress is compressive. For fibrillar Si swarf which is partially amorphous, the residual stress from the crystalline component is tensile. This result is in-line with swarf produced during diamond turning of Si wafers which also shows a downshift in the Raman frequencies from its unstressed position [12,13]. Within the swarfs sampled, crystalline particles with tensile stresses (second quadrant) or amorphous particles with compressive stresses (fourth quadrant) could not be found.

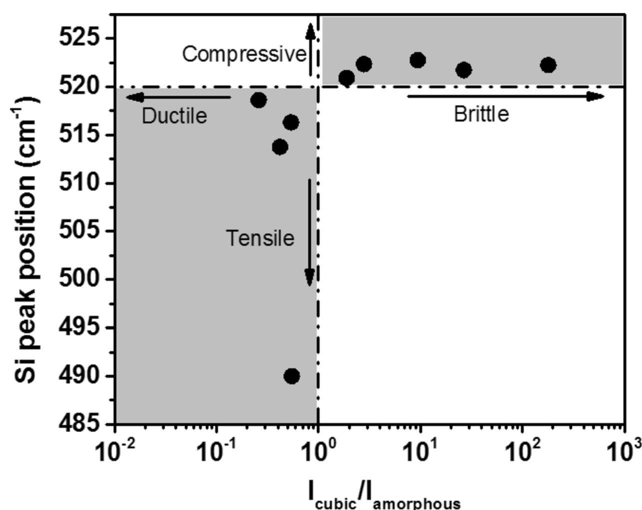

Fig. 3 Stress-phase mapping of nine individual Si swarf particles reveal that crystalline swarf associated with compressive stress and brittle machining are confined to quadrant I. On the other hand, amorphous swarf associated with tensile stress and ductile machining are confined to quadrant III

These trends provide insights into the interaction of diamond microparticles with Si ingot. We propose that as diamonds press against the Si ingot, compressive stresses exceed the fracture strength of Si and result in brittle fracture. This results in particulate Si swarf formation.

On the other hand, as diamonds slide across the kerf, shear stresses remove Si and fibrillar swarf is formed. Shear forces are determined by velocity of wire, size, and shape of individual diamond microparticles which in turn determine rake and clearance angles between diamond and Si and the depth of cut. The downshift in peak position implies residual tensile stresses of the fibrillar swarf particles. This stress could be generated as metallic Si relaxes to Si III/XII and amorphous Si phases. In the following section, the role of diamond microparticles in determining the nature of swarf is discussed.

4.4 Modeling results

Figure 4a shows the force required to move the diamond indenter into Si ingot by 0.01 μm (constant penetration) for four different values of indenter tip radii: 0.1, 0.2, 0.4, and 0.8 μm. Sharp tips require less force, but as these tips become blunt (perhaps due to the cutting action), the normal force needed to achieve the same penetration inside Si increases. This implies that if the force remains constant, blunt diamonds are not able to effectively cut deep into Si.

When a sharp tipped diamond microparticle scratches the surface of a brittle material such as Si, relatively high hydrostatic pressure develops beneath the indenter leading to local plastic deformation zone (Fig. 4a, inset). Tensile stress fields

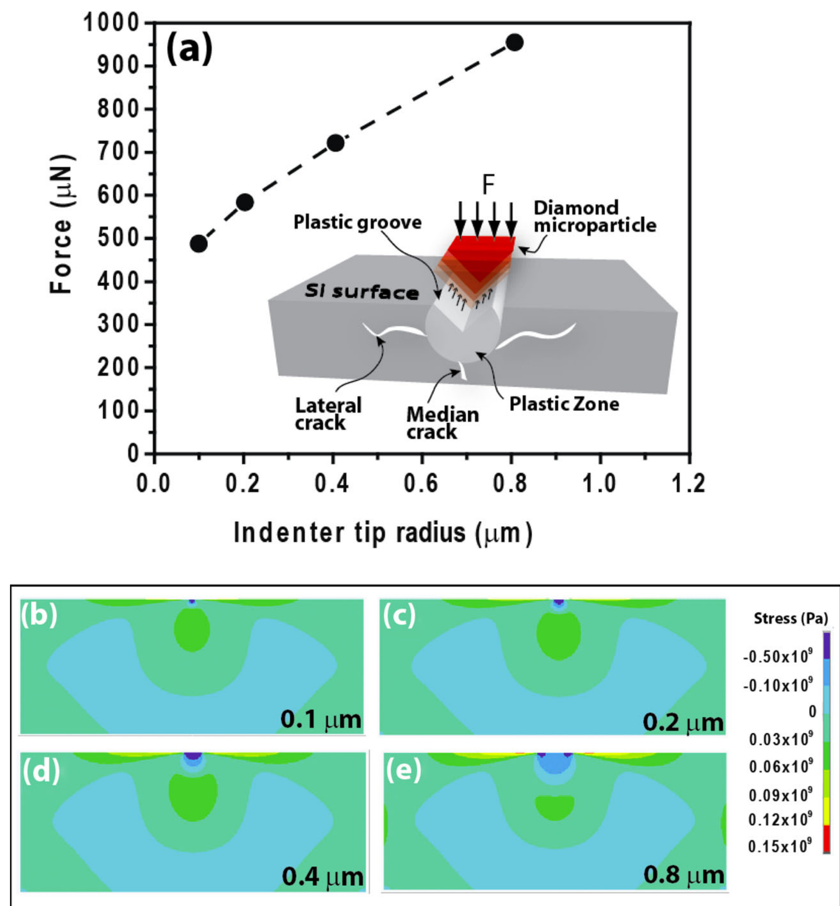

Fig. 4 **a** Variation of force required with diamond indenter tip radius to penetrate 0.1 μm in Si. The *inset* shows the plastic grove formed on the Si surface and generation of lateral and median cracks. **b**–**e** Results from finite element analysis from sharpest (0.1 μm) to bluntest (0.8 μm) diamond tip show the largest region of compressive force (*deep blue*) under the tip and tensile force generation laterally outwards (*yellow* and *red regions*)

surrounding this plastic core can result into two different types of cracks, which initiate at the edge of the plastic zone and propagate radially outward [31]. These are known as (i) lateral cracks and (ii) median cracks. The lateral cracks propagate laterally and upward toward the free surface. The material in the plastic zone between the lateral cracks and the free surface is separated and removed as partially amorphous Si and as narrow, fibrillar particles. On the other hand, when shallow median cracks form, the connection to free surfaces and other cracks can occur via connection to lateral cracks and as a result, the removed Si is mostly in the form of particulate swarf.

Figure 4b–e shows the first principal stress or maximum tensile stress contours inside Si for indenter tip radii of 0.1, 0.2, 0.4, and 0.8 μm, respectively. The tip radii variation represents gradual wear of diamond microparticles as it cuts through Si. Two effects can be observed. First, the tensile stress fields near the surface which have the potential to initiate shallow lateral cracks and the size of the potential plastic zone which is under compression both grow. This implies that the volume of amorphous, fibrillar particles should increase as the indenter tip radius increases (i.e., as the diamonds become dull). Second, as diamond microparticles become dull (i.e., as the tip radius increases), the high tensile stress zone with median cracks moves farther away from the surface, making it less likely for a crack to connect with the surface and generate particulate swarf. This implies that the volume of crystalline, particulate swarf should decrease as diamonds become dull.

Besides constant penetration models, constant force models have also been developed (not shown). This scenario is practically relevant during DCW sawing as the ingots are usually pressed on the DCW webbed frame to produce a normal, reactionary force between the diamond and the Si (Fig. 1a). As the diamonds turn blunt upon usage, the ingot has to be pressed harder against the DCW webbed frame to maintain the same cutting rate (=5 μm/s).

For the simulation, a force of 485.8 μN was applied on 0.1-, 0.2-, 0.4-, and 0.8-μm sharp diamond tips and the penetration depths in Si were monitored. This is the force that is required to push the 0.1-um sharp diamond tip into Si by 0.01 um. The penetration depths obtained were 0.01, 0.0084, 0.0067, and 0.0051 μm, respectively. It was observed that the higher tension in the regions with median crack, directly beneath the plastic zone, gradually disappears as the diamond tip radius increases, indicating that brittle fractures are not likely to happen for blunt tips. In other words, higher forces are needed for blunt tips to induce brittle fracture.

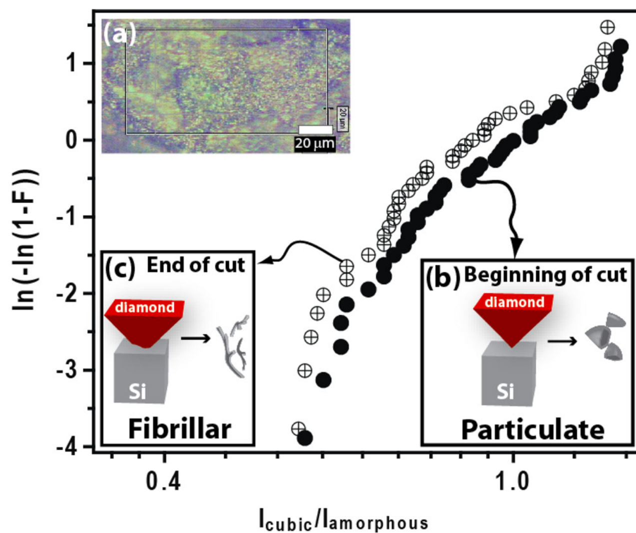

Fig. 5 Weibull plot of $I_{cubic}/I_{amorphous}$ from Raman for swarf collected at the beginning of the cut (•) vs. swarf collected at the end of the same cut (⊕). The blunting of the diamond particles can be statistically discerned as a shift in the $I_{cubic}/I_{amorphous}$ ratio towards lower values (i.e., higher fibrillar fraction). *Insets* show microscope image of swarf powder (*a*) and schematic of the blunting process and its impact on the nature of the Si swarf (*b* and *c*)

The conclusions from both approaches (i.e., constant penetration and constant force), using finite element modeling, are in-line with recent modeling results reported for single grit diamond interaction with Si surfaces using extended-finite element method-based model [32]. These results show that blunt tips are responsible for surface cracks at the ductile to brittle transition zone. Therefore, diamond microparticle wear in DCW leads to generation of fibrillar swarf, provided high pressure is maintained at the diamond-Si interface.

4.5 Model validation using Raman analysis of swarf powder

In order to validate modeling results, Si swarf powder was analyzed. Swarf powder was placed under the Raman microscope objective at 5× magnification and the Raman laser rastered on a 120 μm × 160 μm area (Fig. 5—inset a). The beam focused on a 20-μm × 20-μm area for every single data point. In this way, 48 data points per swarf powder sample were obtained.

Two swarf samples were analyzed. First, swarf powder generated by a new spool of DCW at the beginning of a Si ingot cutting process was obtained. Here, the expectation was that diamond microparticles will be sharp. Second, swarf was obtained from the end of the same Si ingot cutting process. We note that DCW spools are tens of kilometers long. Therefore, it was ensured that the same length segment of DCW performed the entire cut. The expectation was that the same diamond microparticles would be blunted through the course of the cut. The ratio of $I_{cubic}/I_{amorphous}$ for each of the two swarf samples was plotted as a Weibull distribution. Edge outliers were screened from the distribution to focus on results from the median population.

The Weibull plot of $I_{cubic}/I_{amorphous}$ is shown in Fig. 5 for the beginning and end of the cut. It can be seen that $I_{cubic}/I_{amorphous}$ is statistically higher in value for the beginning than for the end of the cutting process. This implies that the fraction of cubic phase (i.e., particulate swarf) is higher at the beginning of the process. As cutting proceeds to completion, diamonds on DCW are possibly blunted and the ratio of $I_{cubic}/I_{amorphous}$ decreases. The fraction of amorphous phase (i.e., fibrillar swarf) increases. This data is in-line with the modeling work described in the previous section.

Clear evidence of the blunting of diamond particles is shown in Fig. 6. Here, representative wire cross sections are obtained via optical microscopy for three DCWs. In Fig. 6a, as-received and fresh DCW is shown. A proprietary metal coating protects the attached diamond particles. In Fig. 6b, a partially used DCW is shown with a diamond particle exposed and its sharp facets intact. This diamond has undergone removal of the protective metal coating and has actively participated in the cutting process. In Fig. 6c, a cross section of a fully worn DCW with diamonds still attached to the steel core is shown. The particles are now degraded and blunt. It is also possible that some diamonds are lost during sawing and could be present in the Si swarf. However, results using Raman to detect the presence of a few diamond particles in Si swarf have been inconclusive. Thus, while DCW has sharp diamonds to begin with, over time blunting of diamonds takes place.

The collective implications for these results are the following. First, Weibull curves such as those provided in Fig. 5

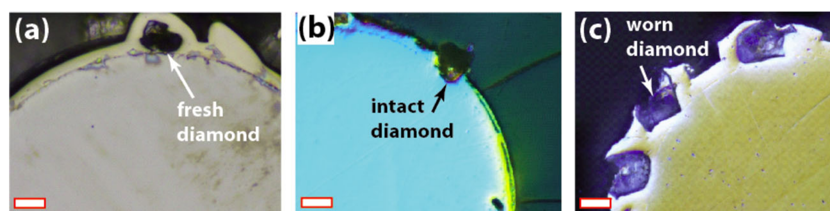

Fig. 6 Cross section of DCW showing **a** as-received, fresh DCW with protective coating over diamond particles, **b** partially used DCW with exposed diamond particle, and **c** fully used DCW with worn diamond on the surface. *Scale bar* represents 10 μm in all images

parameterize the distribution of cubic (i.e., particulate, crystalline swarf) to amorphous (i.e., fibrillar swarf) phases in a powdered swarf sample. Second, the parameter $I_{cubic}/I_{amorphous}$ reflects the *collective* cutting efficiency of millions of diamond microparticles embedded on a DCW. Finally, the change in $I_{cubic}/I_{amorphous}$ represents the *drop* in collective cutting efficiency of the diamond microparticles as they get blunt over time.

5 Conclusions

Quantitative "fingerprinting" of the DCW process using micro-Raman analysis of Si swarf particles has been demonstrated. It is shown that the ratio of cubic to amorphous peak of Si swarf indirectly represents the collective cutting ability of diamond microparticles. As the diamond microparticles increasingly turn blunt, the ratio of cubic to amorphous phases in Si swarf decreases and can be used to track DCW cutting efficiency and quality over time.

Second, it is shown that Si swarf particles can now be categorized as (1) particulate, i.e., crystalline Si with residual compressive stresses and indicative of brittle machining, or (2) fibrillar, i.e., partially amorphous Si with residual tensile stresses indicative of ductile machining. With the additional advantage of Raman as a quick and nondestructive test, it is proposed that this analytical technique can be effectively applied to DCW sawing processes for in situ diagnostics.

Acknowledgments Partial support under the US-India Partnership to Advance Clean Energy-Research (PACE-R) for the Solar Energy Research Institute for India and the United States (SERIIUS), funded jointly by the U.S. Department of Energy (Office of Science, Office of Basic Energy Sciences, and Energy Efficiency and Renewable Energy, Solar Energy Technology Program, under Subcontract DE-AC36-08GO28308 to the National Renewable Energy Laboratory, Golden, Colorado), and the Government of India, through the Department of Science and Technology under Subcontract IUSSTF/JCERDC-SERIIUS/2012, is acknowledged. Partial support for M.H. from NSF CMMI Grant No. 1641111 is acknowledged. The support from Singamaneni Group at Washington University in St. Louis is acknowledged. Optical microscopy was performed in the Flores lab and is acknowledged.

References

1. Luque A, Hegedus S (2011) Handbook of photovoltaic science and engineering, 2nd edn. Wiley, Chichester
2. J.I. Bye, L. Norheim, B. Holme, O. Nielsen, S. Steinsvik, S.A. Jensen, G. Fragiacomo, I. Lombardi, Industrialised diamond wire wafer slicing for high efficiency solar cells, in: H. Ossenbrink, A. Jager-Waldau, P. Helm (Eds.) Proceedings of the 26th European International Conference on Photovoltaic Solar Energy, 2011, pp. 956–960.
3. J. Bye, S.A. Jensen, F. Aalen, C. Rohr, O. Nielsen, B. Gaumann, J. Hodsden, K. Lindemann, Silicon slicing with diamond wire for commerical production of PV wafers, in: 24th European photovoltaic solar energy conference, Hamburg, 2009, pp. 1269–1272.
4. I. Lombardi, G. Fragiacomo, C. Zehetmeier, J. Bye, O. Nielsen, C. Rohr, B. Gaumann, A. Kunzli, High yield recylcing process of silcion kerf from diamond wire wafering, in: 24th European photovoltaic solar energy conference Hambrug, 2009, pp. 1256–1258.
5. Arif M, Rahman M, San WY (2012) A state-of-the-art review of ductile cutting of silicon wafers for semiconductor and microelectronics industries. Int J Adv Manuf Technol 63:481–504
6. Arefin S, Li XP, Cai MB, Rahman M, Liu K, Tay A (2007) The effect of the cutting edge radius on a machined surface in the nanoscale ductile mode cutting of silicon wafer. Proc Inst Mech Eng B J Eng Manuf 221:213–220
7. Arefin S, Li XP, Rahman M, Liu K (2007) The upper bound of tool edge radius for nanoscale ductile mode cutting of silicon wafer. Int J Adv Manuf Technol 31:655–662
8. Li XP, He T, Rahman M (2005) Tool wear characteristics and their effects on nanoscale ductile mode cutting of silicon wafer. Wear 259:1207–1214
9. Liu K, Li XP, Rahman M, Neo KS, Liu XD (2007) A study of the effect of tool cutting edge radius on ductile cutting of silicon wafers. Int J Adv Manuf Technol 32:631–637
10. Uddin MS, Seah KHW, Rahman M, Li XP, Liu K (2007) Performance of single crystal diamond tools in ductile mode cutting of silicon. J Mater Process Technol 185:24–30
11. Cai MB, Li XP, Rahman M (2007) High-pressure phase transformation as the mechanism of ductile chip formation in nanoscale cutting of silicon wafer. Proc Inst Mech Eng B J Eng Manuf 221:1511–1519
12. Jasinevicius RG, Duduch JG, Montanari L, Pizani PS (2012) Dependence of brittle-to-ductile transition on crystallographic direction in diamond turning of single-crystal silicon. Proc Inst Mech Eng B J Eng Manuf 226:445–458
13. Pizani PS, Jasinevicius R, Duduch JG, Porto AJV (1999) Ductile and brittle modes in single-point-diamond-turning of silicon probed by Raman scattering. J Mater Sci Lett 18:1185–1187
14. Komanduri R, Chandrasekaran N, Raff LM (1998) Effect of tool geometry in nanometric cutting: a molecular dynamics simulation approach. Wear 219:84–97
15. Yan JW, Syoji K, Tamaki J (2003) Some observations on the wear of diamond tools in ultra-precision cutting of single-crystal silicon. Wear 255:1380–1387
16. Holt A, Thogersen A, Rohr C, Bye J, Helgesen G, Nordseth O, Jensen SA, Norheim L, Nielsen O (2010) Surface structure of mono-crystalline silicon wafers produced by diamond wire sawing and by standard slurry sawing before and after etching in alkaline solutions. 2010 35th IEEE Photovoltaic Specialists Conference. doi:10.1109/pvsc.2010.5614103
17. Sopori B, Devayajanam S, Shet S, Guhabiswas D, Basnyat P, Moutinho H, Gedvilas L, Jones K, Binns J, Appel J (2013) Characterizing damage on Si wafer surfaces cut by slurry and diamond wire sawing. 2013 IEEE 39th Photovoltaic Specialists Conference. doi:10.1109/pvsc.2013.6744298
18. Wu H, Melkote SN, Danyluk S (2012) Mechanical Strength of Silicon Wafers Cut by Loose Abrasive Slurry and Fixed Abrasive Diamond Wire Sawing. Adv Eng Mater 14:342–348
19. Yu X, Wang P, Li X, Yang D (2012) Thin Czochralski silicon solar cells based on diamond wire sawing technology. Sol Energy Mater Sol Cells 98:337–342
20. Yang J, Banerjee S, Wu J, Myung Y, Rezvanian O, Banerjee P (2016) Phase and stress evolution in diamond microparticles during diamond-coated wire sawing of Si ingots. Int J Adv Manuf Technol 82:1675–1682
21. Lewis IR, Edwards HGM (2001) Handbook of Raman spectroscopy : from the research laboratory to the process line. Marcel Dekker, New York

22. Gogotsi Y, Baek C, Kirscht F (1999) Raman microspectroscopy study of processing-induced phase transformations and residual stress in silicon. Semicond Sci Technol 14:936–944
23. Hopcroft MA, Nix WD, Kenny TW (2010) What is the Young's Modulus of Silicon? J Microelectromech Syst 19:229–238
24. Domnich V, Gogotsi Y (2001) Handbook of surfaces and interfaces of materials (Series Editor, Hari S. Nalwa). Academic, San Diego
25. Hull R (2006) Properties of Crystalline Silicon. Institution of Electrical Engineers, London
26. Properties of Crystalline Silicon (1999) emis Datareviews series, vol 20. Inspec, Institution of Electrical Engineers, London, United Kingdom
27. Dewolf I (1996) Micro-Raman spectroscopy to study local mechanical stress in silicon integrated circuits. Semicond Sci Technol 11: 139–154
28. Dewolf I, Maes HE, Jones SK (1996) Stress measurements in silicon devices through Raman spectroscopy: bridging the gap between theory and experiment. J Appl Phys 79:7148–7156
29. Kailer A, Gogotsi YG, Nickel KG (1997) Phase transformations of silicon caused by contact loading. J Appl Phys 81:3057–3063
30. Domnich V, Gogotsi Y, Dub S (2000) Effect of phase transformations on the shape of the unloading curve in the nanoindentation of silicon. Appl Phys Lett 76:2214–2216
31. Lawn B, Wilshaw R (1975) Indentation Fracture - Principles And Applications. J Mater Sci 10:1049–1081
32. Hao W, Melkote SN (2012) Study of ductile-to-brittle transition in single grit diamond scribing of silicon: application to wire sawing of silicon wafers. J Eng Mater technol 134(4):041011 (041018 pp.)-041011 (041018 pp.). doi:10.1115/1.4006177